N O T E

Generalized simultaneous multi-orientation 2D imaging

Nikolai J. Mickevicius[1] [ID] | **Andrew S. Nencka**[2] | **Eric S. Paulson**[1,2]

[1]Department of Radiation Oncology, Medical College of Wisconsin, Milwaukee, WI, USA

[2]Department of Radiology, Medical College of Wisconsin, Milwaukee, WI, USA

Correspondence
Nikolai J. Mickevicius, Department of Radiation Oncology, Medical College of Wisconsin, 8701 Watertown Plank Road, Milwaukee, WI 53226, USA.
Email: nmickevicius@mcw.edu

Purpose: Flexibility in slice prescription is critical for precise motion monitoring during MR-guided therapies. Adding more slices to improve spatial coverage during rapid 2D cine imaging often hampers temporal resolution. This work describes a framework to simultaneously acquire multiple arbitrarily oriented slices which share a common frequency encoding axis. This framework allows for higher frame rates for a given number of slices compared to conventional interleaved-slice multi-orientation cine imaging.

Theory and Methods: A framework to calculate zeroth gradient moments to be played out between sequentially excited slices with multiple orientations is described here. Experiments were performed in phantom, and in vivo in the head/neck and abdomen of patients.

Results: Images arbitrarily rotated relative to one another were successfully obtained in phantom and in vivo. Simultaneous multi-orientation (SMO) images were also acquired with additional in-plane acceleration to demonstrate the capability of this method to rapidly image objects moving with physiological motion.

Conclusions: The technical feasibility of the generalized SMO imaging framework was tested in this study. It shows promise for continued development for motion monitoring during MR-guided therapies.

K E Y W O R D S

MR-guided radiation therapy, oblique, simultaneous multislice, simultaneous multi-orientation, SMO, SMS

1 | INTRODUCTION

The noninvasive treatment of diseases with radiation therapy often offers improvements in healthcare outcome when used in conjunction with surgical procedures.[1,2] Unfortunately, along with the advantages of noninvasive therapy, come large uncertainties in the position of the target relative to the distribution of the planned dose.[3] Medical imaging plays a substantial role in improving the precision of these therapies. In external beam radiation therapy, for example, the current standard of care involves imaging the patient with on-board cone beam computed tomography (CT) with nondiagnostic quality, and aligning it to a higher quality CT on which the radiation dose plan was generated.[4] While this alignment minimizes setup uncertainties from day to day, uncertainties can also arise when internal anatomy deviates from alignment while the treatment is being delivered. Issues arise when a patient's alignment deviates from the planned dose distribution while the treatment is being delivered.

This misalignment can occur frequently during radiation therapy of abdominal or thoracic tumors. Respiratory motion, organ filling, and bulk motion of the patient due to muscle

relaxation or anxiety occurring within a treatment fraction all have the potential to affect the outcome.[5-7] Common methods to manage this nuisance motion include gating based on external surrogates for respiratory motion, planar real-time X-ray imaging, implanted radiofrequency transponders, and ultrasound imaging. While such techniques have been proven to be functional,[8] each suffers from its own disadvantage. One such disadvantage, for example, is that motion surrogate signals do not always reflect true tumor motion.[9,10] The emergence of MRI-guided radiation therapy (MR-gRT) with integrated imaging and therapy systems[11-14] affords a more robust solution to manage large intrafraction motions.

Rapid two-dimensional "cine" imaging with a high frame rate is employed during MR-gRT for patients exhibiting significant anatomical displacement during respiration. With the high soft tissue contrast in these images, the target can be segmented in real-time.[15] Subsequently, if the target leaves a predefined margin, the beam can be switched off to minimize the risk of toxicity to healthy tissues. The issue with imaging only in a single 2D plane, however, is that out-of-plane motion of the target is difficult to detect. Thus, some real-time imaging solutions on such MR-gRT devices propose the use of interleaved cine imaging in two orthogonal planes to obtain a pseudo-3D estimate of the target motion while maintaining a reasonable frame rate.[16]

The disconnect observed between sequentially measured orthogonal images, as pictured in Preiswerk et al[17] and Mickevicius et al,[18] precludes the simultaneous use of interleaved images from both planes to accurately estimate the position of the target in 3D. Furthermore, as more interleaved slices are added, the effective frame rate for each of the slices is reduced. This led to the development the simultaneous orthogonal plane imaging (SOPI) MRI pulse sequence.[19] SOPI employs simultaneous multislice (SMS) magnetic resonance imaging methodology to spatially encode slices in two orthogonal planes concurrently. Since the orthogonal images are simultaneously measured, robust 3D motion estimates of large structures can be made using images in both planes simultaneously.[19] It was demonstrated that up to a 30% increase in temporal resolution is achievable with SOPI compared to conventional interleaved orthogonal slice approaches.[19] Furthermore, this technology has led to the development and in vitro validation of a radiation dose accumulation technique, which aims to calculate the dose distributions actually delivered to the patient in the presence of irregular respiratory motion.[20] Furthermore, the combination of SOPI and super-resolution approaches afford the synchronous acquisition of the cine imaging necessary for real-time treatment guidance and an isotropic 4D-MRI (3D plus respiratory phase) for retrospective dose accumulation.[21]

Here, we describe a novel MRI framework to generalize the principles of SOPI to permit the simultaneous acquisition of arbitrarily oriented slices which share one common axis. The technical feasibility of this so-called simultaneous multi-orientation (SMO) imaging framework is tested in phantom and in vivo with a radiofrequency spoiled steady-state free-precession implementation. SMO is expected to offer an increasing improvement in temporal resolution as a function of the number of slices to be imaged compared with conventional interleaved-slice cine imaging.

2 | THEORY

Consider N arbitrarily rotated slices sharing a frequency encoding direction to be imaged simultaneously. As in simultaneous image refocusing (SIR)[22] or SOPI[19] acquisitions, the slices are excited sequentially. Therefore, each slice begins accruing phase due to the application of gradients at the isocenter of its radiofrequency (RF) excitation pulse, $T_{ISO,n}$. Here, $n = 1, 2, \ldots, N$ represents the index to the nth slice to be excited.

The simultaneous encoding of the arbitrarily oriented slices simply involves balancing the 0th gradient moment, $M_{0,n}(t)$, for all slices. The 0th moment is the integral of the time-dependent 3×1 gradient vector, $G(t)$, beginning from $T_{ISO,n}$ (Equation 1).

$$M_{0,n}(t) = \int_{T_{ISO,n}}^{T_{ISO,n}+t} G(t')dt' \tag{1}$$

The coordinates in which the gradient moment can be referenced includes those of the physical gradient coils themselves (ie, x, y, and z), or logical coordinates corresponding to the different encoding dimensions of a 2D Cartesian MR imaging experiment (ie, phase encoding (P), frequency encoding (F), and slice-select (S) dimensions). The conversion between logical and physical coordinates is performed by multiplication with a 3×3 orthogonal rotation matrix for each slice, R_n. These matrices are calculated by the vendor given scanner coordinates, patient orientation, slice orientation, and desired phase and frequency encoding dimensions.[23]

$$\begin{bmatrix} M_{0,n,x} \\ M_{0,n,y} \\ M_{0,n,z} \end{bmatrix} = R_n \begin{bmatrix} M_{0,n,P} \\ M_{0,n,F} \\ M_{0,n,S} \end{bmatrix} \tag{2}$$

The hat accent will be used to denote vectors in physical coordinates while no accent denotes vectors in logical coordinates (eg, $\hat{M}_{0,n} = R_n M_{0,n}$).

The 0th gradient moment is related to the well-known k-space coordinate in MRI by the relationship $k_n = \gamma M_{0,n}$, where γ is the gyromagnetic ratio in Hz/T. The step size in k-space along the phase and frequency encoding dimensions is given by $\Delta k_P = 1/FOV_P$ and $\Delta k_F = 1/FOV_F$, respectively, where FOV is the field-of-view along each direction. The acquisition matrix dimensions for the phase and frequency

encoding directions are given by L_P and L_F, respectively. The index $\ell = -L_P/2, \ldots, L_P/2 - 1$ references the phase encoding lines to be acquired.

By the echo time for each slice, TE_n, the 0th gradient moment should be $\boldsymbol{M}_{0,n}(TE_n) = \begin{bmatrix} \ell \Delta k_P/\gamma & 0 & 0 \end{bmatrix}^T$. For each slice, the desired encoding moment, in logical coordinates, immediately prior to the start of the readout gradient is given by (Equation 3):

$$\boldsymbol{E}_{n,\ell} = \begin{bmatrix} \ell \Delta k_P/\gamma \\ M_{0,n,F} \\ 0 \end{bmatrix} \quad (3)$$

The moment accumulated by the start of the readout gradient along the frequency encoding dimension, $M_{0,n,F}$, is dependent on the SMO readout scheme. If an extended readout gradient like those in SIR acquisitions is employed, the slices can be acquired with equal (ETE) or non-equal (NETE) echo times. In the ETE-SIR scheme, the gradient echoes for all slices are acquired in the order in which they were excited under separate portions of the same readout gradient. For NETE-SIR, the signals from all slices are acquired in the opposite order in which they were excited. If a SIR readout is not employed, the signals from all slices will be acquired in a superimposed fashion, inherently with different echo times for each slice (NETE-ALIASED). $M_{0,n,F}$ is calculated as follows for each scheme (Equations 4-6):

$$M_{0,n,F}^{\text{ETE-SIR}} = -(n - 0.5) \cdot L_F \cdot \Delta k_F/\gamma - \delta M_{0,F} \quad (4)$$

$$M_{0,n,F}^{\text{NETE-SIR}} = -(N - n + 0.5) \cdot L_F \cdot \Delta k_F/\gamma - \delta M_{0,F} \quad (5)$$

$$M_{0,n,F}^{\text{NETE-Aliased}} = -0.5 \cdot L_F \cdot \Delta k_F/\gamma - \delta M_{0,F} \quad (6)$$

Here, $\delta M_{0,F}$ is the area under the ramp-up portion of the readout gradient. It is worth noting that, with the ETE-SIR readout scheme, the slices will only have equal echo times if the time in between gradient echoes is equal to the time between isocenters of consecutive RF pulses (ΔT_{RF}). Therefore, the readout bandwidth, BW, must be set accordingly as $BW_{\text{ETE}} = L_F/\Delta T_{\text{RF}}$.

In order to realize the constraint in Equation 3 for all slices, a set of physical coordinate 0th gradient moments played out immediately following the nth slice-selection gradient, $\hat{\boldsymbol{\beta}}_{n,\ell}$, are defined. See Figure 1 for an example $N = 3$ visualization of the $\hat{\boldsymbol{\beta}}_{n,\ell}$ gradient moments. Since the nth slice accumulates phase due to all gradients played out after $T_{ISO,n}$, the following equation describes the relationship between the desired encoding moment and the $\hat{\boldsymbol{\beta}}_{n,\ell}$ moment to be calculated (Equation 7):

$$\begin{bmatrix} \boldsymbol{R}_1 \boldsymbol{E}_{1,\ell} \\ \boldsymbol{R}_2 \boldsymbol{E}_{2,\ell} \\ \vdots \\ \boldsymbol{R}_N \boldsymbol{E}_{N,\ell} \end{bmatrix} - \begin{bmatrix} f_1 \boldsymbol{I} & \boldsymbol{I} & \ldots & \boldsymbol{I} \\ & f_2 \boldsymbol{I} & \ldots & \boldsymbol{I} \\ & & \ddots & \vdots \\ 0 & & & f_N \boldsymbol{I} \end{bmatrix} \begin{bmatrix} \boldsymbol{R}_1 \boldsymbol{\alpha}_1 \\ \boldsymbol{R}_2 \boldsymbol{\alpha}_2 \\ \vdots \\ \boldsymbol{R}_N \boldsymbol{\alpha}_N \end{bmatrix}$$
$$= \begin{bmatrix} \boldsymbol{I} & \boldsymbol{I} & \ldots & \boldsymbol{I} \\ & \boldsymbol{I} & \ldots & \boldsymbol{I} \\ & & \ddots & \vdots \\ 0 & & & \boldsymbol{I} \end{bmatrix} \begin{bmatrix} \hat{\boldsymbol{\beta}}_{1,\ell} \\ \hat{\boldsymbol{\beta}}_{2,\ell} \\ \vdots \\ \hat{\boldsymbol{\beta}}_{N,\ell} \end{bmatrix} \quad (7)$$

Here, $\boldsymbol{I}$ is the 3×3 identity matrix, $\boldsymbol{\alpha}_n$ is a logical coordinate vector containing the total area under the nth slice-select gradient (ie, $\boldsymbol{\alpha}_n = \begin{bmatrix} 0 & 0 & A_{S,n} \end{bmatrix}^T$), and f_n is the fraction of the total 0th gradient moment for the nth slice-select gradient occurring after $T_{ISO,n}$. If Equation 7 is written as $\boldsymbol{Y} = \boldsymbol{A}\boldsymbol{B}$, then a solution for the $\hat{\boldsymbol{\beta}}_{n,\ell}$ moments can be obtained via $\boldsymbol{B} = (\boldsymbol{A}^T\boldsymbol{A})^{-1}\boldsymbol{A}^T\boldsymbol{Y}$, or recursively starting with $n = N$ and substituting backward toward $n = 1$. Since $\boldsymbol{A} \in \mathbb{R}^{3N \times 3N}$, the solution to $\boldsymbol{Y} = \boldsymbol{A}\boldsymbol{B}$, in general, costs $(3N)^3$ floating point operations. With modern host computers, it is highly feasible to calculate these moments in real-time for each TR period. To ensure consistency with an established multi-orientation pulse sequence, the generalized SMO framework was used to derive the equations from the SOPI publication.[19] This derivation is shown in the Supporting Information.

A constant spoiling gradient moment is desired within every repetition time (TR) for spoiled steady-state free precession pulse sequences. This helps to remove transverse magnetization coherences and eliminate spatially dependent spoiling. The spoiling moments, $\boldsymbol{S_n} = \begin{bmatrix} S_{n,P} & S_{n,F} & S_{n,S} \end{bmatrix}^T$, are the total 0th moments accumulated between TR periods. These moments need not be equal for all slices. They only need to be constant within each TR and have a magnitude, $|S_n| = \sqrt{S_{n,P}^2 + S_{n,F}^2 + S_{n,S}^2}$, large enough to sufficiently dephase the transverse magnetization. A minimum phase dispersion of 4π across each voxel is commonly used while calculating dephasing gradient moments.[24] In an attempt to fulfill the condition in Equation 8, the end-of-TR gradients with physical 0th moment of $\hat{\boldsymbol{\Omega}}_\ell$ were introduced.

$$\boldsymbol{M}_{0,n}(T_{ISO,n} + \text{TR}) = \boldsymbol{S_n} \quad (8)$$

As an ansatz, the $\hat{\boldsymbol{\Omega}}_\ell$ moments are calculated to satisfy Equation 8 for the first (ie, $n = 1$) slice. Since the moment needed to fulfill this condition for subsequent slices is dependent on the $(j + 1)$th phase encoding moment, a perfect balancing for all slices is not feasible. However, it was shown a posteriori that the logical slice and phase spoiling components for slices $n \geq 2$ remain constant and relatively close to zero such that the spoiling moment along the frequency encoding direction largely
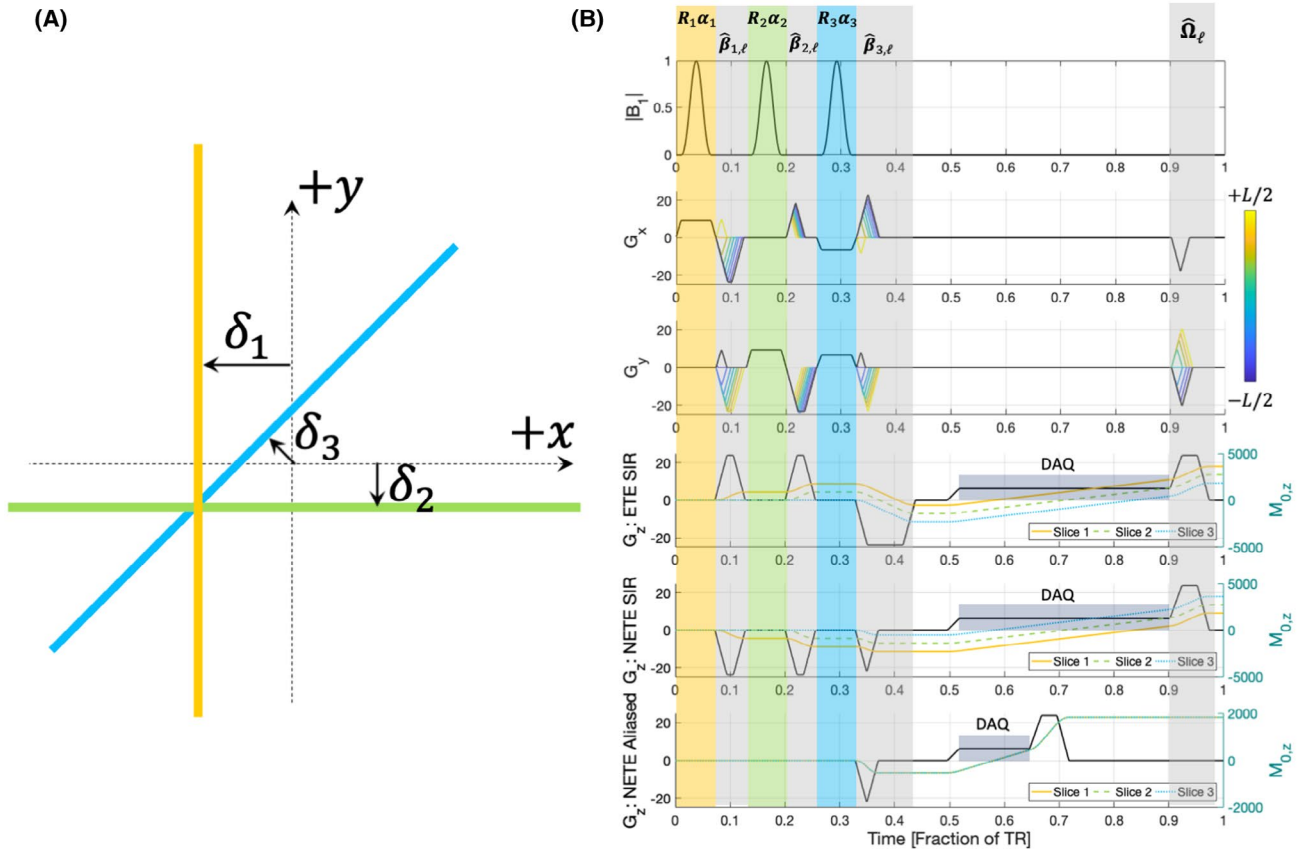
FIGURE 1 Simultaneous multi-orientation pulse sequence. A, Example of SMO slice prescription. Each slice shares a common frequency encoding axis. The off-isocenter distance for each slice is given by δ_n. B, SMO pulse sequence diagram. Gradients immediately following each excitation pulse along the slice-select and phase encoding dimensions (eg, x and y) are dependent on the current phase encoding line. The zeroth gradient moments referred to within the text are labeled above the pulse sequence timing diagram. Three frequency encoding (G_z) schemes are shown. In the simultaneous image refocusing (SIR) readouts, each slice is separately refocused under different portions of extended readout gradient. In the aliased readout, the gradient echoes for all slices completely overlap. The echo times for each can be seen where the $M_{0,z}(t)$ plots for each slice reach a value of zero. In the equal echo time (ETE) scheme, the echo times for all slices are equal. All slices have different echo times in the non-equal echo time (NETE) schemes. The data acquisition (DAQ) window is labeled on the plateau of the readout gradient

dominates the net spoiling area (See Supporting Information Figure S1). The expression for the end-of-TR gradient moment in physical coordinates is shown in Equation 9.

$$\hat{\mathbf{\Omega}}_\ell = \mathbf{R}_1 \mathbf{S}_1 - \hat{\beta}_{1,\ell} - \sum_{i=2}^{N} \left(\mathbf{R}_i \boldsymbol{\alpha}_i + \hat{\beta}_{i,\ell} \right) \qquad (9)$$

In this study, the following spoiling moments were employed: $S_{1,P} = 0$, $S_{1,F} = \frac{8\pi}{\Delta z \gamma}$ and $S_{1,S} = 0$, where Δz is the voxel size along the frequency encoding dimension. A complete list of all variable definitions used in this section can be found in the Supporting Information.

3 | METHODS

The SMO pulse sequence was implemented on a 3T Siemens Magnetom Verio (Siemens Healthineers, Erlangen,

Germany). Both RF and gradient spoiling were employed to obtain fast low angle shot (FLASH) contrast. Each excitation pulse was calculated with a Hanning-windowed Sinc envelope, a 600 μs duration, and a bandwidth of 2 kHz.

An imaging experiment in a cylindrical phantom was first performed. The phantom was oriented with the longitudinal axis of the cylinder parallel to the y-axis of the scanner. Slices were prescribed with the frequency encoding direction along the z-axis. SMO FLASH scans were performed with two, three, and four simultaneous orientations (ie, $N = [2, 3, 4]$). In each case, the angle of rotation about the z-axis between each slice orientation was equal to $90°/(N-1)$. With such slice prescriptions, two identical slices (ie, coronal and sagittal) are acquired for each value of N. These acquisitions were repeated for ETE-SIR, NETE-SIR, and NETE-ALIASED readout schemes. No in-plane acceleration was employed. A scan-specific deep learning-based k-space interpolation, known as Slice-RAKI was used to separate the NETE-ALIASED images.[25] The calibration data required to train the 4-layer Slice-RAKI network

were acquired for each slice individually by switching off the RF pulses for the other slices in the SMO FLASH pulse sequence. The specifics of the RAKI convolutional neural network training can be found in the Supporting Information. The NETE-ALIASED data were acquired with CAIPIRINHA shifts of FOV/N between slices.[26] Common imaging parameters include a slice thickness of 5 mm, matrix size of $L_P = L_F = 128$, bandwidth of 81.5 kHz. The TR values for $N = [2,3,4]$ were 8.3, 12.0, and 15.6 ms, respectively. The echo times for each readout scheme and slice are shown in Supporting Information Table S1. The FOV for the phantom scan was 240×240 mm.

The above experiments were repeated in a head and neck and abdomen of two cancer patients who consented to be a part of an institutional review board approved study. Additionally, to demonstrate the capability to acquire high-frame rate imaging with SMO, data prospectively accelerated with $N = 2$ and an in-plane acceleration factor of $R = 3$ were acquired in vivo using an NETE-ALIASED readout. A TR of 5.1 ms was prescribed for these highly accelerated scans. These data were reconstructed using two-step RAKI (ie, separate slice and in-plane interpolation).[25,27] The FOVs for the head and neck and pancreas patients were 300×300 and 340×340 mm, respectively. The effective frame rate for each of these scans was approximately 4.6 frames per second. The number of RF coils used for the phantom, head/neck, and abdomen scans were 21, 16, and 24, respectively.

To demonstrate the advantages of SMO over conventional interleaved-slice imaging, the maximum achievable temporal resolutions were compared. If L_P phase encode lines are desired for all slices, then the total acquisition time for a single frame of interleaved imaging will be equal to $T_{ILV} = N \cdot L_P \cdot \mathrm{TR}_{ILV}$. For SMO, the acquisition time will be $T_{SMO} = L_P \cdot \mathrm{TR}_{SMO}$. If fixed prescription geometry and pulse sequence constraints (eg, minimum echo time, RF pulse duration, readout/slice bandwidths, maximum gradient slew rate, and maximum gradient amplitude) are considered, then the relative temporal acceleration factor achieved with SMO is given by $R_{T,N} = T_{ILV}/T_{SMO} = N \cdot \mathrm{TR}_{ILV}/\mathrm{TR}_{SMO}$, where the TR values are the shortest possible repetition times for each case. $R_{T,N}$ was

calculated for $N = [2, 3, 4]$ for each readout scheme using the prescription geometry from the phantom experiments.

4 | RESULTS

The SMO images for the phantom, head/neck, and abdomen can be seen in Figures 2-4, respectively. Reconstructed images for all values of N for the abdomen and head/neck experiments can be found in Supporting Information Figures S3 and S4. The differences in orientation can be seen in the transition from coronal to sagittal sections in the phantom and each anatomical site. From the phantom scan (Figure 2), it is apparent that very high spatial frequencies along the readout dimension leak through into other slices. The severity of this high spatial frequency leak is higher in the structural phantom than in the in vivo images. Also apparent in both the in vivo and phantom datasets are partial saturation bands occurring at the intersection of the slices. The width of the saturated regions appears to increase with N.

Differences in image contrast are evident between the ETE-SIR, NETE-SIR, and NETE-ALIASED images. These differences are expected given the different echo times between acquisitions, T_2^* decay, and the chemical shift between water and fat. These differences are best visualized in the sagittal slice in the $N = 2$ head and neck acquisition between the ETE-SIR and NETE-SIR readouts (Supporting Information Figure S3).

The results of the NETE-ALIASED experiments are presented in Figures 2-4. The simultaneously acquired multi-orientation images are shown prior to slice separation. The CAIPIRINHA FOV shifts between the slices are evident in the slice-aliased images. The images separated using Slice-RAKI are depicted in subsequent columns. The unaliased images exhibit image quality on par with those acquired using the SIR readout without the high spatial frequency leak. Small amounts of residual aliasing in the $N = 4$ phantom images can be seen due to imperfect slice separation. However, these Slice-RAKI reconstructions still out-perform those of parallel imaging algorithms in terms of noise enhancement and
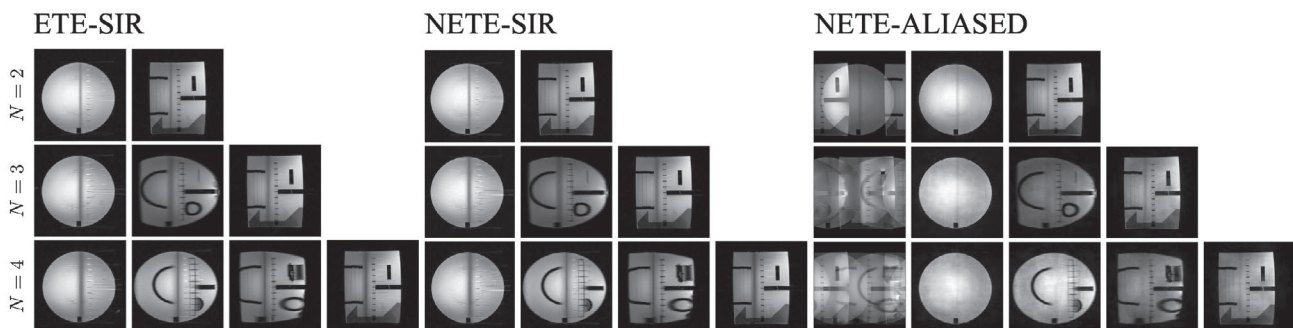
FIGURE 2 Phantom SMO results. Equal-TE (ETE), non-equal-TE (NETE), and NETE with an aliased readout images are shown from left to right for different values of N. The obliquity of the rotated slices can be seen with the transition from a circular to a rectangular cross-section of the cylindrical phantom. The aliased images were reconstructed using Slice-RAKI

FIGURE 3 Head and neck SMO results. Equal-TE (ETE), non-equal-TE (NETE), and NETE with an aliased readout images are shown for $N = 4$. The aliased images were reconstructed using Slice-RAKI. See Supporting Information Figure S3 for head and neck SMO reconstructions at all values of N

residual aliasing (See Supporting Information Figure S2 for the parallel imaging reconstructions).

The RAKI reconstructions of the in-plane accelerated SMO images with the NETE-ALIASED readouts are shown in Figure 5. Despite higher noise than the datasets acquired without in-plane acceleration, these images would still be of sufficient quality for visualizing the approximate position of a target, or organ containing a target, in the presence of physiological motion such as swallowing or respiration.

The temporal acceleration factors for SMO compared with conventionally interleaved-slice imaging can be seen in Supporting Information Table S2. Values of $R_{T,N} > 1$ represent an improvement in the achievable frame rate compared to interleaved imaging. Although $R_{T,N,\text{ETE}}$ was trending toward a value of one as N increased, SMO did not provide any frame rate advantages for ETE readout schemes. For NETE imaging with a SIR readout, SMO provided an improvement in frame rate for $N = 4$. NETE imaging with an aliased readout provides large improvements in frame rate for all values of N. The use of SMO with an aliased readout scheme provided between 47% ($N = 2$) and 100% ($N = 4$) improvements in frame rate relative to interleaved imaging.

5 | DISCUSSION

In this work, the principles of SIR were generalized to the simultaneous acquisition of data from multiple slices with different orientations. Preliminary experiments showed the technical feasibility of such an imaging framework.

The high spatial frequency leak between slices when using a SIR readout is likely because the readout periods for each slice under the extended gradient are not separated by any crushers. An implementation of SMO with crushed pathways, as in Krafft et al,[28] would help to mitigate these artifacts if separate readout periods are desired for each slice. Otherwise, the high spatial frequency slice leak is eliminated by the NETE-ALIASED readout at the expense of noise enhancement and/or residual aliasing due to imperfect slice separation. The saturation bands are not as apparent in the NETE-ALIASED phantom images. This effect has been attributed to the RAKI reconstruction, which was trained on k-space data from images without saturation bands. Additionally, the short T_1 of the phantom in combination with use of the low flip angle FLASH sequence may be the reason why this effect was not as prominent in vivo.
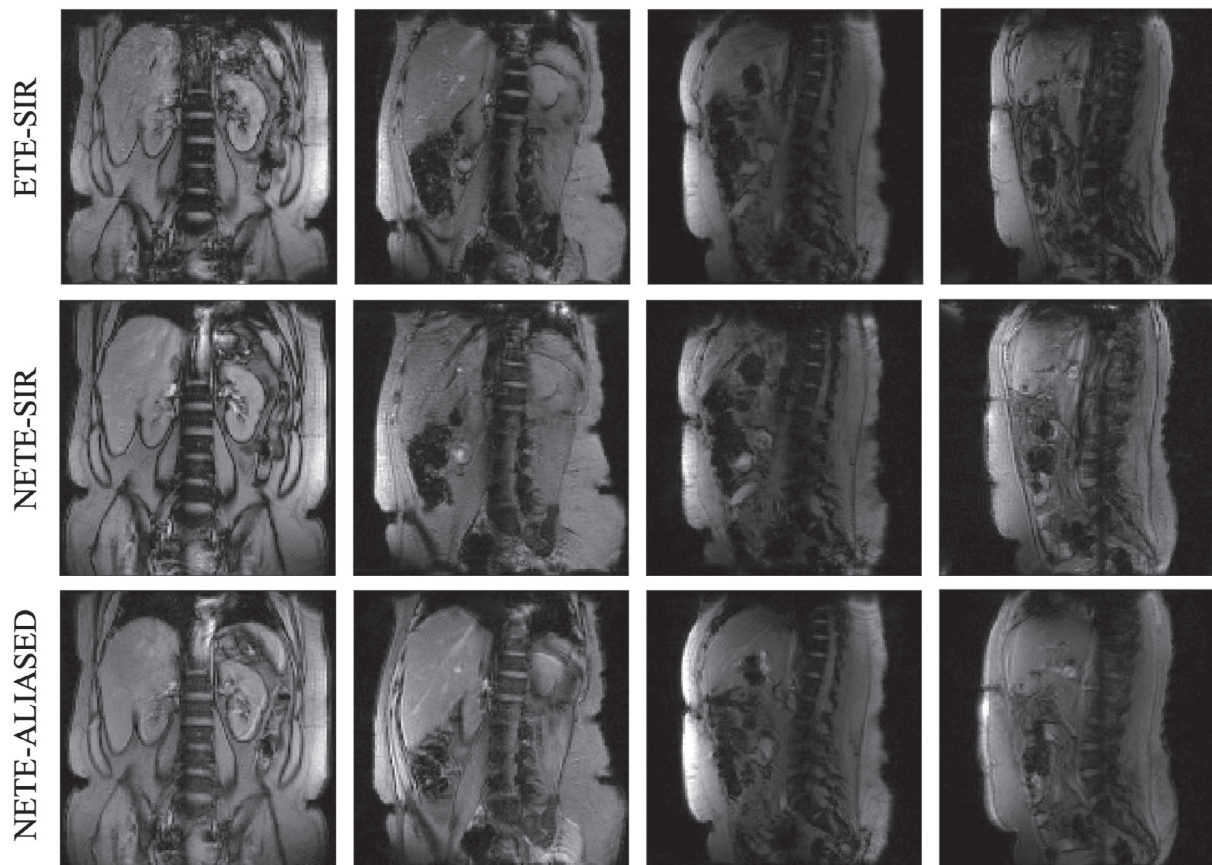
FIGURE 4 Abdominal SMO results. Equal-TE (ETE), non-equal-TE (NETE), and NETE with an aliased readout images are shown for $N = 4$. The aliased images were reconstructed using Slice-RAKI. See Supporting Information Figure S4 for abdominal SMO reconstructions at all values of N

The primary advantage of SMO over conventional interleaved-slice imaging is the capability of increasing the cine imaging frame rate while keeping the number of slices the same. It was determined, despite the longer minimum TRs with SMO, that the improvements in frame rate increase with N, particularly for the NETE-ALIASED readout scheme. This is mainly because only a single gradient spoiling and phase-rewinding period (ie, Ω_ℓ) is required per TR for each group of N slices. For $N = 4$, the time needed to acquire all desired phase encoding lines for all slices was calculated half of that for conventional interleaved imaging. The time saving advantages of NETE-ALIASED SMO come with a few drawbacks. First, there is a lack of contrast flexibility with SMO. The required use of gradient spoiled steady-state free precession pulse sequences results in a lack of T_2-weighted contrast, like those in balanced SSFP acquisitions, which may be desirable in some applications. Second, with the use of NETE imaging, there are also some inconsistencies in contrast between slices from the same acquisition. This may not be desirable, particularly if one slice has in-phase water and fat signals while they are out-of-phase in other slices. Third, SMO introduces artifacts due to imperfect slice separation, particularly when also accelerating the acquisition in-plane.

As seen in Figure 5, some residual aliasing and noise are introduced with in-plane accelerated SMO reconstruction, even when using the noise-robust Slice-RAKI neural network.

The imperfect slice separation seen in the parallel imaging reconstructions of the NETE-ALIASED data in the Supporting Information are due to g-factor penalties on the SNR, which depend on coil geometry and acceleration factor.[29] While the SNR of the parallel imaging reconstructions could be improved by decorrelating the data to have unit noise variance,[30] the use of the deep learning-based RAKI reconstructions in this work was able to qualitatively improve the quality of the individual multi-orientation images. There was an increase in computational burden with RAKI compared with parallel imaging methods. It took approximately 2 minutes to train each slice separating network on a single CPU. These networks need only be trained once for the cine imaging data, and the application of the model to prospectively accelerated data is very fast (<50 ms). The use of a GPU is expected to substantially reduce the computation times for reconstruction.

It was previously demonstrated that a single Slice-RAKI network can robustly be applied to data from multiple respiratory motion states.[25] As long as the position of the slices does not need to be adjusted, Slice-RAKI appears to be a good
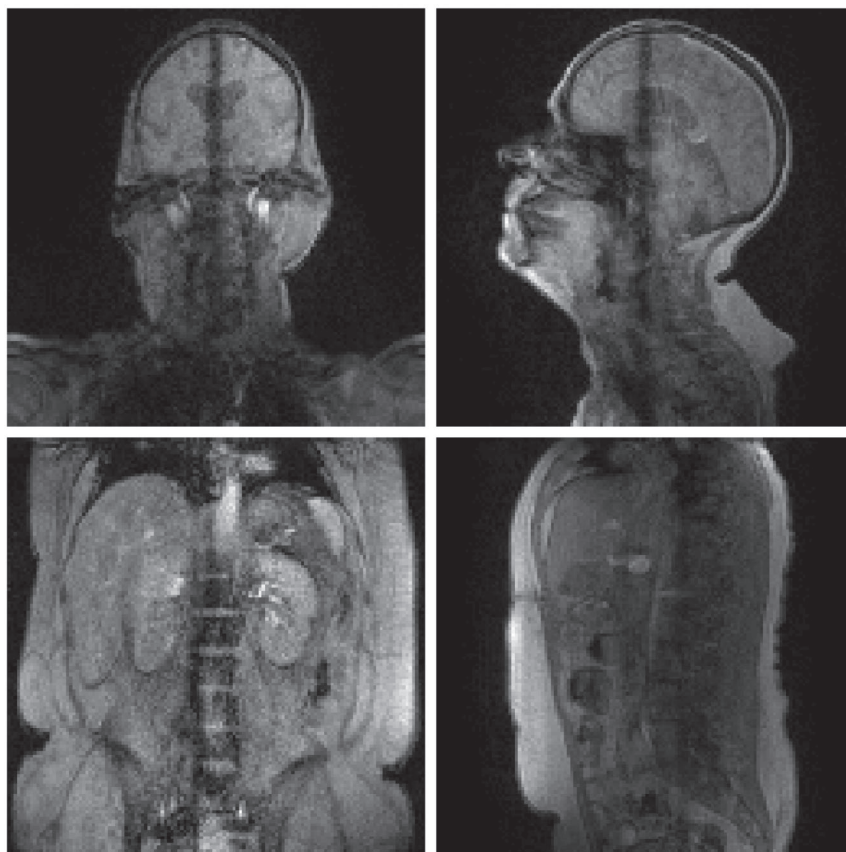
FIGURE 5 SMO Head/neck and abdominal cine results. $N = 2$ NETE-ALIASED SMO cine imaging with an additional in-plane acceleration factor of $R = 3$. Example coronal and sagittal frames reconstructed with Slice-RAKI are shown in the head/neck (top) and abdomen (bottom)

choice for separation of the SMO data. For some MR-guided interventions, however, the capability to re-position slices in real time is necessary. This precludes the use of RAKI for such applications as significant calibration data acquisition times and network re-training times would hinder the intervention.

In addition to rapid dynamic imaging for MR-guided therapeutic applications, SMO could also find use in the rapid acquisition of "scout" or "localizer" scans performed at the beginning of a diagnostic MR exam. Furthermore, imaging in multiple orientations is seen in cardiac and musculoskeletal MR imaging.[31,32] SMO may be used to accelerate the acquisition of data for such multi-orientation scans.

In the context of online tumor tracking during MR-guided radiation therapy, the size of the tumor plays a role in determining the number of cine imaging planes that can be used. Even for interleaved imaging, partial saturation regions exist at the intersection of the slices,[33] which can obstruct the visualization of small tumors and lead to the use of only a single plane for small targets. Ultimately, the number of cine imaging planes used during treatment is left to the discretion of the treating physician. In order to determine whether SMO is suitable for online tumor tracking, a rigorous study relating tumor size and respiratory trajectory to the optimal number of orientations, slice thickness, and in-plane resolution of SMO and interleaved imaging should be performed on a combined high field MRI and linear accelerator.

The SMO framework provides a unique acquisition paradigm capable of rapidly acquiring multi-planar imaging. SMO may find use in respiratory motion monitoring during MR-guided radiation therapy. In this application, multi-orientation imaging is often necessary to visualize the intra-fraction motion of the therapy target and nearby organs at risk. SMO can provide not only the cine imaging necessary for real-time motion monitoring, but also dynamic volumes for retrospective dose accumulation, if slice position modulations like those seen in Ref. [20] are employed. This extension of SMO will be the subject of future investigation.

ORCID
Nikolai J. Mickevicius http://orcid.org/0000-0003-3826-6667

REFERENCES
1. Lindberg RD, Martin RG, Romsdahl MM, Barkley Jr. HT. Conservative surgery and postoperative radiotherapy in 300 adults with soft-tissue sarcomas. *Cancer*. 1981;4710:2391–2397.
2. Bernier J, Domenge C, Ozsahin M, et al. Postoperative irradiation with or without concomitant chemotherapy for locally advanced head and neck cancer. *New England J Med*. 2004;35019:1945–1952.
3. Van Herk M. Errors and margins in radiotherapy. *Semin Radiat Oncol*. 2004;14:52–64.
4. Ahunbay EE, Peng C, Chen GP, et al. An on-line replanning scheme for interfractional variations a. *Med Phys*. 2008;358:3607–3615.

5. Bortfeld T, Jokivarsi K, Goitein M, Kung J, Jiang SB. Effects of intra-fraction motion on IMRT dose delivery: statistical analysis and simulation. *Phys Med Biol*. 2002;4713:2203.

6. Shirato H, Seppenwoolde Y, Kitamura K, Onimura R, Shimizu S. Intrafractional tumor motion: lung and liver. *Semin Radiat Oncol*. 2004;14;10–18.

7. Litzenberg DW, Balter JM, Hadley SW, et al. Influence of intra-fraction motion on margins for prostate radiotherapy. *Int J Radiat Oncol* Biol* Phys*. 2006;652:548–553.

8. Kubo HD, Hill BC. Respiration gated radiotherapy treatment: a technical study. *Phys Med Biol*. 1996;411:83–91.

9. Feng M, Balter JM, Normolle D, et al. Characterization of pancreatic tumor motion using cine MRI: surrogates for tumor position should be used with caution. *Int J Radiat Oncol Biol Phys*. 2009;743:884–891.

10. Goldstein SD, Ford EC, Duhon M, McNutt T, Wong J, Herman JM. Use of respiratory-correlated four-dimensional computed tomography to determine acceptable treatment margins for locally advanced pancreatic adenocarcinoma. *Int J Radiat Oncol* Biol* Phys*. 2010;762:597–602.

11. Lagendijk JJ, Raaymakers BW, van Vulpen M. The magnetic resonance imaging-linac system. *Semin Radiat Oncol*. 2014;243:207–209.

12. Mutic S, Dempsey JF. The ViewRay system: magnetic resonance-guided and controlled radiotherapy. *Semin Radiat Oncol*. 2014;243:196–199.

13. Fallone BG. The rotating biplanar linac-magnetic resonance imaging system. *Semin Radiat Oncol*. 2014;243:200–202.

14. Keall PJ, Barton M, Crozier S. The Australian magnetic resonance imaging-linac program. *Semin Radiat Oncol*. 2014;243: 203–206.

15. Bourque AE, Bedwani S, Carrier JF, et al. Particle filter–based target tracking algorithm for magnetic resonance–guided respiratory compensation: robustness and accuracy assessment. *Int J Radiat Oncol* Biol* Phys*. 2018;1002:325–334.

16. Seregni M, Paganelli C, Lee D, et al. Motion prediction in MRI-guided radiotherapy based on interleaved orthogonal cine-MRI. *Phys Med Biol*. 2016;612:872–887.

17. Preiswerk F, Toews M, Cheng CC, et al. Hybrid MRI-Ultrasound acquisitions, and scannerless real-time imaging. *Magn Reson Med*. 2017;78:897–908.

18. Mickevicius NJ, Paulson ES. Simultaneous orthogonal plane cine imaging with balanced steady-state free-precession contrast using kt GRAPPA. *Phys Med Biol*. 2018;6315:15NT02.

19. Mickevicius N, Paulson E. Simultaneous orthogonal plane imaging. *Magn Reson Med*. 2017;78:1700–1710.

20. Mickevicius NJ, Chen X, Boyd Z, Lee HJ, Ibbott GS, Paulson ES. Simultaneous motion monitoring and truth-in-delivery analysis imaging framework for MR-guided radiotherapy. *Phys Med Biol*. 2018;6323:235014.

21. Mickevicius NJ, Paulson ES. Simultaneous acquisition of orthogonal plane cine imaging and isotropic 4D-MRI using super-resolution. *Radiotherapy Oncol*. 2019;136:121–129.

22. Feinberg DA, Reese TG, Wedeen VJ. Simultaneous echo refocusing in EPI. *Magn Reson Med*. 2002;48:1–5.

23. Edelman RR, Stark DD, Saini S, et al. Oblique planes of section in MR imaging. *Radiology*. 1986;1593:807–810.

24. Bernstein MA, King KF, Zhou XJ. *Handbook of MRI Pulse Sequences*. Burlington, MA: Academic Press; 2004.

25. Mickevicius NJ, Paulson ES, Tugan Muftuler L, Nencka AS. Application of a k-Space interpolating artificial neural network to in-plane accelerated simultaneous multislice imaging. arXiv e-prints 2019;arXiv:1902.08589.

26. Breuer FA, Blaimer M, Heidemann RM, Mueller MF, Griswold MA, Jakob PM. Controlled aliasing in parallel imaging results in higher acceleration (CAIPIRINHA) for multi-slice imaging. *Magn Reson Med*. 2005;53:684–691.

27. Akçakaya M, Moeller S, Weingärtner S. Uğurbil K. Scan-specific robust artificial-neural-networks for k-space interpolation (RAKI) reconstruction: database-free deep learning for fast imaging. *Magn Reson Med*. 2018;81:439–453.

28. Krafft AJ, Rauschenberg J, Maier F, Jenne JW, Bock M. Crushed rephased orthogonal slice selection (CROSS) for simultaneous acquisition of two orthogonal proton resonance frequency temperature maps. *J Magn Reson Imaging*. 2013;386:1510–1520.

29. Pruessmann KP, Weiger M, Scheidegger MB, Boesiger P. SENSE: sensitivity encoding for fast MRI. *Magn Reson Med*. 1999;42:952–962.

30. Pruessmann KP, Weiger M, Börnert P, Boesiger P. Advances in sensitivity encoding with arbitrary k-space trajectories. *Magn Reson Med*. 2001;46:638–651.

31. Kubo T, Horii M, Harada Y, et al. Radial-sequence magnetic resonance imaging in evaluation of acetabular labrum. *J Orthopaedic Sci*. 1999;4:328–332.

32. Cloos MA, Assländer J, Abbas B, et al. Rapid radial T_1 and T_2 mapping of the hip articular cartilage with magnetic resonance fingerprinting. *J Magn Reson Imaging*. 2018. hrttps://doi.org/10.1002/jmri.26615.

33. Borman P, Bos C, Stemkens B, Moonen C, Raaymakers B, Tijssen R. Assessment of 3D motion modeling performance for dose accumulation mapping on the MR-linac by simultaneous multislice MRI. *Phys Med Biol*. 2019;649:095004.

SUPPORTING INFORMATION

Additional supporting information may be found online in the Supporting Information section.

FIGURE S1 Readout axis dominates the total gradient spoiling moment. As described in the main text, the spoiling gradient areas are calculated to fully rewind the zeroth gradient moment along the logical slice and phase-encoding directions for the first (ie, $n = 1$) slice. This figure provides a sanity check to ensure that the gradient spoiling moment achieved within each TR is largely dominated by the readout axis and to ensure the spoiling is constant over time. The gradient moment accrued within a TR for each slice along the readout dimension ($M_{0,R}$) is divided by the magnitude of the total gradient moment ($|M_0|$) and plotted for consecutive phase encoding line indices, ℓ. The base-10 log of this ratio is very small for all slices for both the ETE and NETE readout schemes. These data were obtained using the POET pulse sequence simulation tool (Siemens Healthineers, Erlangen, Germany) using the exact same parameters as the phantom and brain experiments performed in the main manuscript. The $n = 3$ and $n = 4$ lines overlap in both plots

FIGURE S2 non-equal-TE aliased SMO Results. Non-equal-TE (NETE) SMO results using an aliased readout. The left column shows the slice-aliased images prior to separation. The individual images were separated using the readout-concatenated SENSE-GRAPPA parallel imaging method. These images contain more noise and residual aliasing in the $N = 3$ and $N = 4$ reconstructions than those separated using Slice-RAKI

FIGURE S3 Full Head and Neck SMO Results. Head and neck SMO reconstructions for all readout schemes and numbers of orientations

FIGURE S4 Full Abdominal SMO Results. Abdominal SMO reconstructions for all readout schemes and numbers of orientations

TABLE S1 Echo times in milliseconds for phantom and in vivo SMO experiments for each readout scheme, acceleration factor, and slice number. N is the number of orientations and n is an index counting from 1 to N

TABLE S2 Relative temporal acceleration factors for SMO compared with conventional interleaved slice imaging for each of the three readout schemes